


Surface plasmon enhanced second harmonic behavior of a noncentrosymmetric dolmen-type Au nanostructure

Atsushi Sugita,^{*} Kenshin Muroi, Yohsei Nakatsuka, and Sohta Tamotsu
Faculty of Engineering, Shizuoka University, Hamamatsu, Shizuoka 432-8561, Japan

 (Received 8 June 2023; revised 24 August 2023; accepted 29 August 2023; published 12 September 2023)

This paper presents the second harmonic generation (SHG) behavior of a dolmen-type Au nanostructure under surface plasmon (SP) resonance conditions. The SP-enhanced optical fields of the plasmonic metal nanoparticles are suitable for nonlinear wave mixing at the nanoscale. However, the SP-enhanced fields alone are insufficient for second-order nonlinear optics, including the SHG effect. As in traditional nonlinear optics, it is helpful to prepare the metal nanoparticles in a noncentrosymmetric shape to obtain the large SHG signals in the far fields. The dolmen-type Au nanostructure consists of three centrosymmetric rectangular Au nanorods (AuNRs), two of which are arranged in parallel and the third is perpendicular. The U-shaped arrangement breaks the centrosymmetry in this complex nanostructure. The noncentrosymmetric dolmen-type AuNRs exhibited ~ 25 times higher SHG signals than the reference single AuNR. According to the numerically mapped surface charges and near fields, the enhanced SHG signals were related to the hybridized bonding state between the dipolar plasmon of the monomer moiety and the quadrupolar plasmon of the dimer moiety. The far-field SHG signals are attributed to the intense near field, which was not centrosymmetric in the nanogap region between the monomer and dimer moieties. The dependence of the SHG signals was also investigated as a function of the separation between the monomer and dimer moieties. The SHG conversion efficiency shows a considerable increase as the separation narrows down to $\sim 20\%$ of the AuNR size. Our present research demonstrates that second-order nonlinear plasmonic behavior can be engineered by appropriately arranging the constituent simply shaped metal nanoparticles.

DOI: [10.1103/PhysRevB.108.125412](https://doi.org/10.1103/PhysRevB.108.125412)

I. INTRODUCTION

Metal nanoparticles have been studied for many years for their unique and exotic optical properties [1–4]. Surface plasmons (SPs), which are collective oscillations of conducting electrons, are generated on metal nanoparticle surfaces under light irradiation. When SPs are produced, intense and localized near fields are generated directly above them, which are useful for the nanoscale manipulation of light [5]. The SP resonance wavelength is sensitive to changes in the refractive index of the surrounding optical medium. This property is applied in technologies used for sensing of gas, pH levels, biological materials, etc., [6–8] and can be tuned by engineering the size [9], shape [10], and surrounding environment [11] of the metal nanoparticles.

Complex plasmonic nanostructure systems exhibit a more diverse photonic behavior than single-particle systems [12–14]. When metal nanoparticles are assembled in close proximity, the SP polarizations are coupled by near-field interactions and they oscillate coordinately. In the strong coupling regime, the SP polarizations hybridize to form new modes [15,16]. Their resonance frequencies are shifted with respect to those of the single particles. The arrangement of metal nanoparticles is crucial for the electromagnetic properties of the hybridized SP modes. When properly arranged, the

near fields in the complex systems are more confined and enhanced than in the single-particle systems [17,18]. The resonant wavelength in the former is more sensitive to changes in the refractive index of the surrounding optical medium than in the latter [19]. It is quite natural to extend these properties to a variety of nanophotonic applications as well, of which nonlinear optics (NLO) is one of the most important [20–23].

NLO is a phenomenon of mixing multiple photons, resulting in the generation of photons with sum or difference frequencies. The NLO phenomena tend to occur at very high levels of light intensity. The intense and confined SP-enhanced optical fields are suitable for operating nonlinear wavelength conversions. There are several requirements for better wavelength conversion in nonlinear plasmonics. First, the fundamental wavelength must be tuned to the SP resonance. For further improvement, it is also helpful to tune the wavelength-converted light to a different SP resonance [24].

In traditional NLO, the inversion symmetry of the optical medium has an important effect on the NLO susceptibilities [25]. Odd-order effects are allowed in the optical media of any symmetry, whereas the even-order effects are allowed only in noncentrosymmetric media. A similar selection rule is applied to nonlinear plasmonics [26]. The nonlinear susceptibilities of metal nanoparticles are attributed to the surface and bulk terms [27–29]. The surface term is related to the broken symmetry at the dielectric/metal interface. This behavior is explained by the electric dipole approximation. The bulk term includes the electric quadrupole and magnetic dipole interactions, which

^{*}sugita.atsushi@shizuoka.ac.jp

are allowed even in the centrosymmetric particles beyond the electric dipole approximation. The contribution of the former is much larger than that of the latter [27]. In application of even-order nonlinear plasmonics, it is important to consider how to use the surface terms effectively.

The wavelength conversions resulting from the surface term occur at the surface of metal nanoparticles of any shape. However, it is usually difficult to observe them in the far fields, when the particle shape is centrosymmetric. The NLO polarizations, or the point light sources of new light waves, are distributed over the particle surface in centrosymmetric matter. During the propagation, the emissions cancel each other perfectly. Exceptionally, even-order NLO behavior can be observed even in the centrosymmetric nanoparticle of small size because of the bulk terms. In addition, it can be observed in the far field, when a multipole plasmon mode is generated in a relatively large metal nanoparticle by exploiting the retardation effect under oblique incidence conditions [30,31]. Alternatively, it allows us to access it in the far field by breaking the centrosymmetry of the environment surrounding the centrosymmetric metal nanoparticle [32]. In general, to benefit from the dominant surface term, the metal nanoparticle shapes should be noncentrosymmetric [33].

The concept of complex plasmonic nanostructures is suitable for applications in even-order nonlinear plasmonics. There have been reports of complex plasmonic nanostructures with unique designs. Most have been challenged by dealing with the second harmonic generation (SHG) behavior, one of the most fundamental NLO phenomena [34–37]. In the SHG effect, the two photons in the incident light are combined into one frequency-doubled photon.

Because rectangular rod-shaped nanoparticles are centrosymmetric, they are not suitable for even-order NLO applications. When two nanorods were arranged in a T shape, the centrosymmetry was broken and electric dipole-type nonlinearities were obtained [34]. The nanotrimer structure, which consisted of one large and two small rods in a coaxial arrangement, satisfied the double resonance conditions; the former and the latter rods exhibited SP resonances under fundamental and SHG light illuminations, respectively [35]. Furthermore, the generated SHG signals were approximately four times higher than that of a single nanorod satisfying a single resonance. The dimers consisting of a rod and a V-shaped particle also satisfied the double resonance condition [36]. In addition, the mode-matching condition was satisfied and the two modes satisfying the resonances in response to the fundamental and SHG lights overlapped spatially. The oligomer structure, or clustered nanoparticles, supported the Fano resonance condition, in which the radiation loss is suppressed, resulting in more enhanced near fields [37]. A several-fold enhancement in the SHG conversions was obtained at the Fano resonance of the heptamer structure compared with the conventional plasmonic antenna system.

Herein, the SHG behavior of a dolmen-type Au nanostructure is reported. The structure consisted of three closely assembled rectangular Au nanorods (AuNRs), two of which were arranged in parallel and the third was perpendicular [38]. The centrosymmetry was broken in the dolmen-type nanostructure, although each constituent AuNR was centrosymmetric. Assuming that the fourth AuNR is placed

perpendicular to the two parallel AuNRs and opposite to the third, the system becomes centrosymmetric again. The tetramer is not suitable for the SHG operation. This trimer structure is probably suitable for electric dipole-type second-order NLO operations. The numerical study of Butet and Martin suggested that the SHG responses of the dolmen-type nanostructure are promising as a nanoruler for evaluating distances as small as a few nanometers [39]. The third harmonic generation (THG) behavior of the dolmen-type Au nanostructure was reported by Metzger *et al.* [40]. However, there are still no reports on the experimental data of the even-order NLOs, including the SHG.

The unique behavior of coordinated plasmons has been studied using various spectroscopic techniques, such as conventional optical microscopy [38], electron energy loss spectroscopy [41], cathode luminescence spectroscopy [41,42], and photoelectron emission microscopy [43]. These studies have showed that coordinated plasmons exhibited the characteristics of Fano resonance, which is interference between the broadband electric dipolar plasmon in the monomer moiety and the narrow-band electric quadrupolar plasmon in the dimer moiety [38,41,44]. Conversely, Yu *et al.* explained the coordinated plasmons in terms of plasmon hybridization because the intense photoelectron emission signals were recorded at the positions of the far-field extinction peaks rather than at the Fano dip [43].

First, we investigated the SHG behavior of the dolmen-type Au nanostructure and compared it with that of the reference AuNR monomer and dimer structures to determine if they were really suitable for the second-order NLO operations. The dolmen-type Au nanostructure supports several coordinated plasmon modes that respond differently to the wavelength and polarization direction of the incident light waves. Each mode can be selectively excited by appropriately selecting the wavelength and polarization of the excitation light. The polarization state of the SHG waves can also be sensitive to the plasmon modes, not only toward fundamental wavelengths but also toward the SHG wavelengths. Then, the SHG signals were studied as a function of the wavelength and the polarization direction of the excitation light. The polarization states of the SHG signals were also resolved.

Numerical calculations were performed to obtain the distributions of the surface charges and the near fields near the nanostructures. Additionally, the SHG excitation spectrum was calculated using the nonlinear effective susceptibility method from previous studies [45,46]. Using the extensive experimental and numerical data, we attempted to understand how the near fields are converted into nonlinear polarizations at the AuNR surfaces and how they propagate into the far field. Finally, the SHG signals were studied as a function of the interparticle separation between the monomer and dimer moieties. The efficiency of plasmon coupling depended on the interparticle separation. We used the data to discuss how the near-field coupling strength influences the second-order susceptibilities.

II. EXPERIMENTAL

The dolmen-type Au nanostructures were fabricated on a fused silica substrate by using electron beam lithography

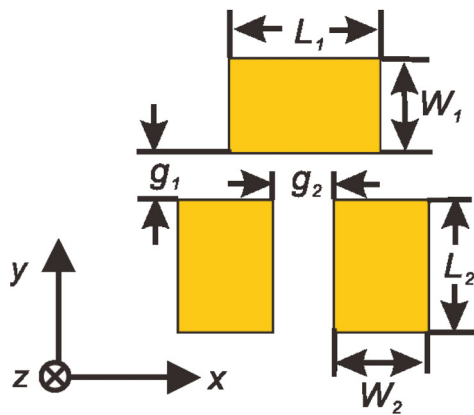
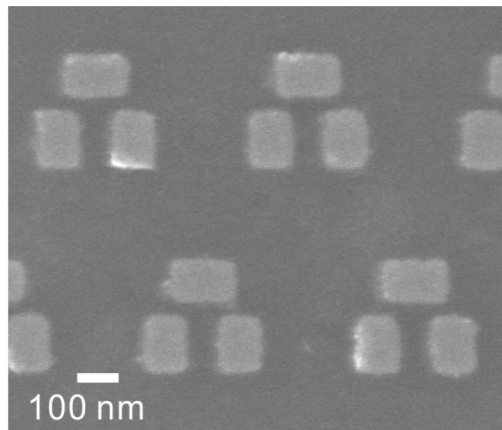


FIG. 1. Scanning electron microscopy (SEM) image of dolmen-type Au nanostructures. The size parameters of L_1 , W_1 , L_2 , and W_2 , and the interparticle separations g_1 and g_2 of the constituent Au nanorods are shown. The definition of the coordinates is also shown.

method. The scanning microscope image of them is shown in Fig. 1. Figure 1 also shows the size parameters of the dolmen-type Au nanostructures, as well as the coordinate definitions. The nanostructures were arranged in a two-dimensional face-centered rectangular lattice or, more precisely, a rhombic lattice. Here, the x axis was set along the long axis of the AuNR in the monomer moiety and the y axis was set along the long axis of the dimer moiety. The length, width, and thickness of the AuNR were $L_1 = 160$ nm, $W_1 = 100$ nm, and $T_1 = 50$ nm, respectively, in the monomer moiety and $L_2 = 140$ nm, $W_2 = 100$ nm and $T_2 = 50$ nm, respectively, in the dimer moiety. Structures with different edge-to-edge separations ($g_1 = 30\text{--}200$ nm) were prepared. The edge-to-edge separations between the two AuNRs were $g_2 = 70$ nm in the dimer moiety. Here, the distances between the neighboring dolmen-type Au nanostructures in the x - and y -axis directions were set to $\Lambda_x = \Lambda_y = 500$ nm to avoid an unexpected diffraction grating effect [45,46]. In two-dimensional metallic nanoparticle systems, the SP resonance can be coupled to the surface lattice resonance, if the operating wavelength is longer than the periodicity. The monomer and the dimer structures were also prepared for comparison.

The linear optical properties of the samples were investigated by measuring the extinction spectra. The light source

was white light from a tungsten lamp. The light beam was shaped by passing it through a multimode optical fiber with a core diameter $\phi \sim 100$ μm . The beam was loosely focused on the sample at normal incidence using a plano-convex lens. The beam diameter on the sample was ~ 100 μm .

The excitation light sources for SHG spectroscopy were femtosecond optical pulses (600 mW average power, 6 nJ pulse energy, and 100 fs pulse width at 75 MHz) from a mode-locked Ti:sapphire laser. The oscillation wavelength was tunable between 730 and 920 nm. The SHG signals were detected in transmission geometry using a back-illuminated charge coupled device (CCD) camera (Pixis: 1024BR, Princeton Instruments Inc.) after being spectrally resolved using a multichannel spectrograph (HRS-500, Princeton Instruments Inc.). A color glass filter (FGB37, Thorlabs Inc.) was used to remove the residual portion of the excitation light that propagated almost collinear with the SHG light. The SHG excitation spectra were obtained by measuring the SHG signals at different excitation wavelengths. The polarization of the excitation light was rotated using a $\lambda/2$ wave plate, whereas the polarization states of the SHG signals were resolved using a Glan-Taylor prism. The beam diameter ϕ on the sample was ~ 100 μm . The average power was 40 mW, corresponding to a peak power of 70 MW/cm².

III. NUMERICAL

The extinction spectra, the surface charge distributions, and the near-field distributions were calculated using the finite-difference time-domain method with the FULLWAVE software (Rsoft Design Group, Inc.). Yee's algorithm was used to solve Maxwell's equation in the time domain [47]. The partial derivatives in space and in time are discretized by means of the central difference approximation. A staggered grid is used in which the electric and magnetic fields are interleaved. A perfectly matched layer condition was established. The simulated regions are 1000, 1000, and 2000 nm in the x -, y -, and z -axis directions, respectively. The meshes were evenly spaced with a pitch of 5 nm. To calculate the extinction spectra, pulsed plane waves were launched vertically onto the surface of the dolmen-type Au nanostructures on a SiO₂ substrate. Monochromatic plane waves were used to calculate the surface charge and the near-field distributions.

The SHG excitation spectra were calculated using the nonlinear effective susceptibility method described in previous studies [48,49]. The method is based on the theory of Lorentz's reciprocity [50]. According to the Lorentz reciprocity theorem, the near-field generation under plane-wave irradiation from the detector and electric field propagation radiated by polarizations on the metal nanoparticle surface to the detector are considered as identical process. The far-field SHG electric field [$E_{\text{SHG}}(2\omega)$] was determined using Eq. (1):

$$E_{\text{SHG}}(2\omega) \propto \int_S \chi_{\perp\perp\perp} \cdot E_{\perp}(\omega, \vec{r})^2 \cdot E_{\perp}(2\omega, \vec{r}) \cdot dS. \quad (1)$$

The integration was performed over the entire surface of the three AuNRs. In Eq. (1), $E_{\perp}(\omega, \vec{r})$ is the near-field component normal to the surface at position \vec{r} generated by the fundamental light at frequency ω . $p_{\text{NLO}}(2\omega, \vec{r}) = \chi_{\perp\perp\perp} \cdot E_{\perp}(\omega, \vec{r})^2$ is the nonlinear polarization generated on

the surface of the metal nanoparticle. $\chi_{\perp\perp\perp}$ is the surface nonlinear susceptibility tensor component of Au, where \perp is the component normal to the surface. $E_{\perp}(2\omega, \vec{r})$ is the near-field component normal to the surface at 2ω driven by the plane wave propagating from the detector. This term is used as a substitute of the scattering rate of the SHG waves generated on the surface of the metal nanoparticle in the far field. $p_{\text{NLO}}(2\omega, \vec{r}) \cdot E_{\perp}(2\omega, \vec{r}) = \chi_{\perp\perp\perp} \cdot E_{\perp}(\omega, \vec{r})^2 \cdot E_{\perp}(2\omega, \vec{r})$ is the spatial-overlap degree between the nonlinear polarization and near field at the SHG wavelength. This term means that the far-field SHG signal is efficiently observed when the $E_{\perp}(\omega, \vec{r})$ and $E_{\perp}(2\omega, \vec{r})$ have good overlap.

According to the selection rule, $\chi_{\perp\parallel\parallel}$ and $\chi_{\parallel\perp\parallel}$ are nonvanishing electric dipole allowed second-order surface susceptibility tensor components. However, a previous study showed that they were much smaller than $\chi_{\perp\perp\perp}$ [27]. Therefore, only the $\chi_{\perp\perp\perp}$ component was included in the calculations. More precisely, this component includes the contribution of the bulk term, which cannot be separated from the surface term. Rather, this term deserves to be referred to as the surfacelike term. The hydrodynamic model provides the explicit form of $\chi_{\perp\perp\perp}$, as shown in Eq. (2) [29,51]:

$$\chi_{\perp\perp\perp} = \frac{1}{4} [\varepsilon_r(\omega) - 1] \cdot \frac{e \cdot \varepsilon_0}{m \cdot \varepsilon(\omega)^2 \cdot \omega^2}. \quad (2)$$

The parameters ε_0 , $\varepsilon(\omega) = \varepsilon_r(\omega) + i\varepsilon_i(\omega)$, m , and e are the permittivity of vacuum, the dielectric function of Au at frequency ω , the electron mass, and the electron charge, respectively. In this definition, the electric fields at the fundamental and SHG wavelengths are evaluated outside the metal region. The data on the dielectric function of Au were taken from the literature [52].

First, the near-field distribution [$E_{\perp}(\omega)$] was calculated at position \vec{r} on the surface of the AuNRs under irradiation of the monochromatic plane wave at the fundamental frequency ω . Next, the surface nonlinear polarization component, $p_{\text{NLO}}(2\omega) = \chi_{\perp\perp\perp} \cdot E_{\perp}(\omega)^2$, was calculated. The near-field distribution [$E_{\perp}(2\omega)$] was also calculated separately for a frequency of 2ω . The values of $E_{\perp}(\omega, \vec{r})$ and $E_{\perp}(2\omega, \vec{r})$ were evaluated just outside the Au on the air/Au interface. Finally, the far-field SHG waves were obtained after performing the integral over the entire surface of the nanostructure. The square of E_{SHG} [Eq. (2)] provides the intensity of the far-field SHG signal.

IV. RESULTS AND DISCUSSION

Figure 2 shows the extinction and SHG excitation spectra of the dolmen-type Au nanostructure. Figures 2(a) and 2(b) are the data for the x - and y -polarized lights, respectively. The spectra of the constituent monomer and dimer structures were studied for reference. The data of the monomer, dimer, and their sum are shown in the figure. There were three peaks in the extinction spectrum of the dolmen-type Au nanostructure in response to the x -polarized light. These three peaks at $\lambda_{X_1} = 908$ nm, $\lambda_{X_2} = 800$ nm, and $\lambda_{X_3} = 737$ nm are referred to as peaks X_1 , X_2 , and X_3 , respectively. Peaks X_1 and X_2 are located at shorter and longer wavelengths with respect to that of the monomer at 835 nm. The peaks correspond to the two

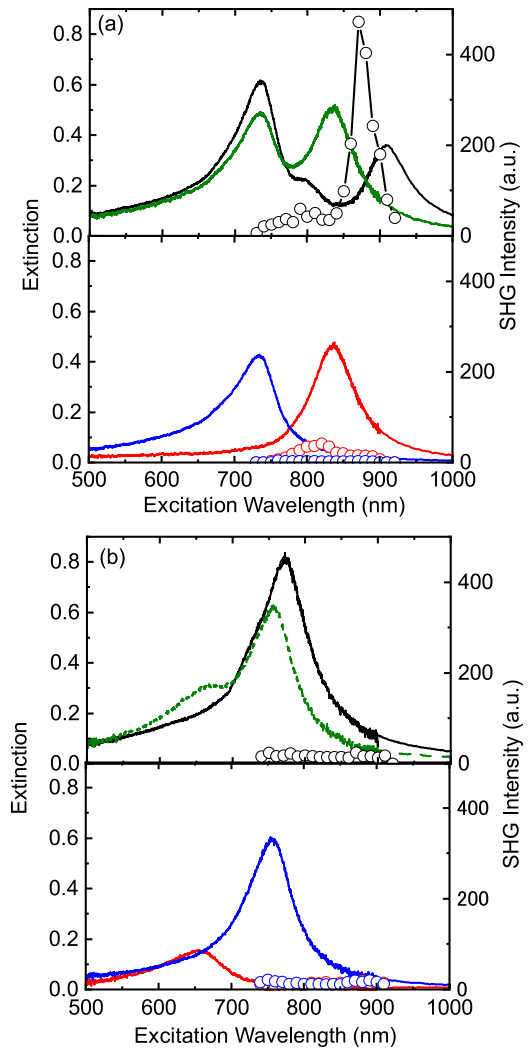


FIG. 2. Extinction (black solid curve) and SHG excitation spectra (black open circles) of the dolmen-type Au nanostructure together with the reference monomer (blue solid curve and open circles) and dimer structure (red solid curve and open circles). The green dashed curve is the sum of the data from the monomer and dimer structures. Graphs (a) and (b) correspond to the data under x - and y -polarized excitation light, respectively.

extinction peaks of the dolmen-type Au nanostructure in the previous study [43].

In the previous study, it was indicated that the two new modes, the bonding and antibonding modes, were formed after the near-field coupling between the dipole mode in the monomer moiety and the quadrupolar mode in the dimer moiety. In the bonding mode, the dipole and the quadrupole oscillate in phase and the resonance condition is satisfied at a wavelength longer than that of the monomer. Conversely, in the antibonding mode, the dipole and quadrupole oscillate out of phase and the resonance condition is satisfied at a wavelength shorter than that of the monomer. Peaks X_1 ($\lambda_{X_1} = 908$ nm) and X_2 ($\lambda_{X_2} = 800$ nm) correspond to the bonding and antibonding modes described in the previous study. Conversely, the wavelength position of peak X_3 was consistent with that of the dimer structure and was related to the plasmon

oscillation along the short axis direction of the AuNRs in the dimer structure.

The dolmen structures show a strong peak at $\lambda'_{X1} = 870$ nm and a weak peak at $\lambda'_{X2} = 790$ nm in the SHG excitation spectra. These two peaks corresponded to peaks X_1 and X_2 in the extinction spectrum. However, the SHG peak wavelength differed from that of the extinction peak in the two peaks. The SHG peak position of X'_1 ($\lambda'_{X1} = 870$ nm) was 38 nm shorter than the extinction peak position of X_1 ($\lambda_{X1} = 908$ nm). Furthermore, the SHG peak position of X'_2 ($\lambda'_{X2} = 790$ nm) was 10 nm longer than the extinction peak position of X_2 ($\lambda_{X2} = 800$ nm). The monomer showed a faint SHG peak at 830 nm. This was a result of the bulk term, which is allowed even for the particles with centrosymmetric shapes. The wavelength of monomer SHG peak was consistent with that of the extinction peak. The dimer showed almost no SHG signals.

The intensity of the SHG peak at $\lambda'_{X1} = 870$ nm was 25 times higher than that of the reference monomer at 800 nm. The SHG intensity at $\lambda'_{X2} = 790$ nm was almost as high as that of the monomer. These results indicate that resonant photoexcitation of the hybridized bonding mode was suitable for the conversion of far-field SHG waves, whereas photoexcitation of the antibonding mode was not.

The average SHG power at the peak λ'_{X1} was $P_{\text{SHG}} = 0.07$ pW at $P_F = 40$ mW-average pump power, corresponding to 70 MW/cm²-peak power. The SHG power conversion efficiencies were $P_{\text{SHG}}/P_F = 0.2 \times 10^{-11}$. The value of the SHG conversion efficiency is almost comparable to that of plasmonic nanostructures in previous studies [53,54].

The extinction peak of the dolmen-type AuNR structure showed two peaks at $\lambda_{Y1} = 772$ nm and $\lambda_{Y2} = 670$ nm under y -polarized light, which are referred to as peaks Y_1 and Y_2 , respectively. The peak at $\lambda_{Y1} = 772$ nm corresponds to the peak at 759 nm of the reference dimer, which was a result of plasmon oscillation along the long axis of the AuNRs. The magnitude of the redshift was $\Delta\lambda_{Y1} = 14$ nm, which was much smaller than $\Delta\lambda_{X1}$ for the x -polarized lights. The redshift was also related to the plasmon coupling between the monomer and dimer moieties. The peak at $\Delta\lambda_{Y2} = 670$ nm corresponded to that of the reference monomer and was caused by the plasmon oscillation along the short axis of the AuNR.

The SHG intensity of the dolmen-type Au nanostructure was as weak as that of the reference monomer and dimer structures for the y -polarized excitations. Although plasmon coupling occurred between the monomer and dimer moieties, this hybridized plasmon did not generate the near fields necessary to convert the far-field SHG. Therefore, not all of the hybridized plasmon modes in the dolmen structure were useful for second-order nonlinear light-matter interactions at the nanoscale.

The polarization states of the SHG waves were studied in the dolmen-type Au nanostructure. Figure 3 shows the polar plot of the SHG signals at $\lambda'_{X1} = 870$ nm against the x -polarized excitations as a function of the angle of the polarizer. The direction of polarization was defined as the angle with respect to the x -axis in Fig. 1. There were two lobes at 90° and 270° , indicating that the SHG waves were y polarized. Therefore, the dolmen-type Au nanostructure converted the x -polarized fundamental light into y -polarized SHG waves.

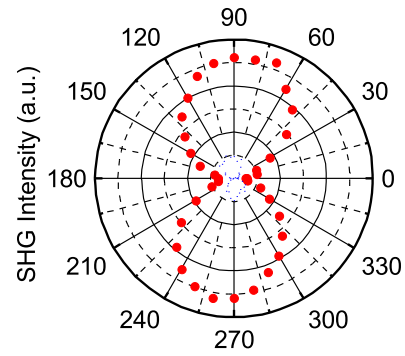


FIG. 3. Polarization resolved SHG signals at 880 nm excitation wavelength.

Next, the numerical data of the extinction and SHG excitation spectra are presented. In the SHG excitation spectrum calculations, the surface integral in Eq. (1) was performed only on the six surfaces of A_1 , A_2 , B_1 , B_2 , C_1 , and C_2 [Fig. 4(a)]. In Fig. 3, the x -polarized excitation light waves were converted into y -polarized SHG waves by the dolmen-type Au nanostructure. As mentioned above, the surface nonlinear susceptibility tensor component, $\chi_{\perp\perp\perp}$, was much larger than the other tensor components and was the only one considered in the calculation. The far-field SHG waves were inevitably attributed to the surface nonlinear polarization component, $p_y(2\omega, \vec{r}) = \chi_{\perp\perp\perp} \cdot E_y(\omega, \vec{r})^2$, generated on these six surfaces. The y -polarized near-field component generated by the x -polarized incident light at frequency 2ω was used as $E_y(\omega, \vec{r})$ in Eq. (1), and the y -polarized component generated by the y -polarized lights at frequency 2ω was used as $E_y(2\omega, \vec{r})$.

In this study, the excitation light was tunable between 730 and 920 nm. The SHG signals were obtained in the wavelength range of 365–460 nm. The present dolmen-type Au nanostructure did not exhibit any SP resonance and $E_y(2\omega, \vec{r})$ was a smooth function of the wavelength in this SHG wavelength range. Therefore, the shape of the SHG excitation spectrum was determined using the near-field waveform in the wavelength region of the excitation light.

Figure 4(b) shows the numerical data of the extinction and SHG excitation spectra of the dolmen-type Au nanostructure against x -polarized light. The data of the reference monomer and dimer structures are also displayed. There were three peaks at $\lambda_{X1} = 935$ nm, $\lambda_{X2} = 780$ nm, and $\lambda_{X3} = 730$ nm in the extinction spectrum of the dolmen-type Au nanostructure. The monomer and dimer structures showed peaks at 830 and 740 nm, respectively. The peaks at $\lambda_{X1} = 935$ nm and $\lambda_{X2} = 800$ nm appeared at longer and shorter wavelengths, respectively, than the 830 nm-peak of the monomer structure. The peak at $\lambda_{X3} = 730$ nm was consistent with that of the dimer structure. These features of the extinction spectrum were reproducible in the experimental data [Fig. 2(a)].

The SHG excitation spectrum had a strong peak at $\lambda'_{X1} = 910$ nm in addition to the weak secondary peak at $\lambda'_{X2} = 790$ nm. The strong X'_1 peak corresponded to the extinction peak of X_1 . However, the former occurred at a shorter wavelength than the latter. The λ'_{X1} position was ~ 15 nm

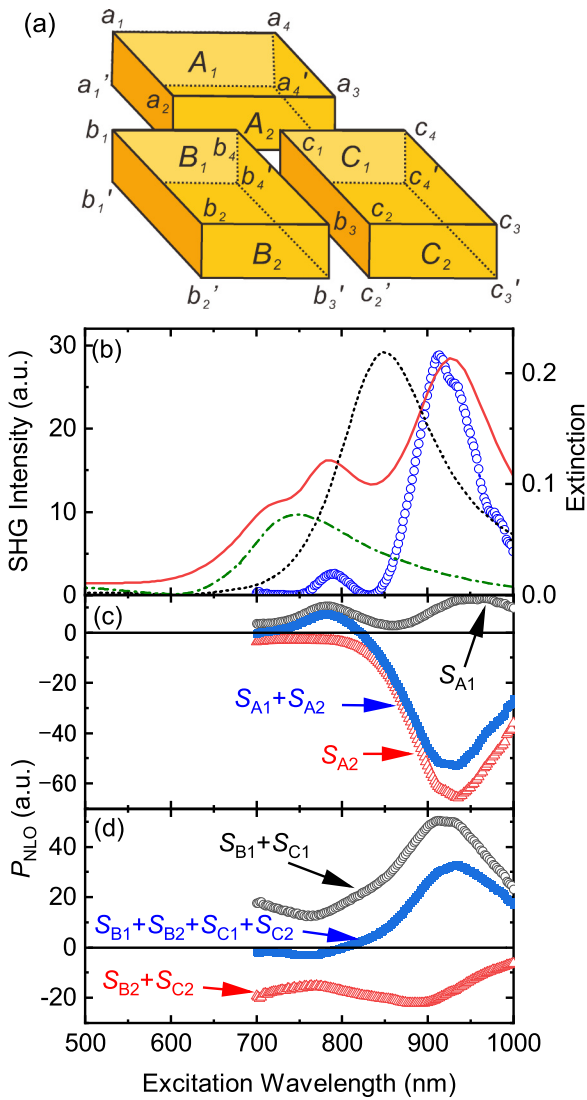


FIG. 4. (a) Definitions of surfaces and edges of a dolmen-type Au nanostructure. (b) Calculated extinction (red solid curve) and SHG excitation (blue open circles) spectra of a dolmen-type Au nanostructure. Extinction spectra of the reference monomer (black dotted curve) and the dimer (green dashed curve) structures are also shown. (c) SHG field components in Eq. (3) from surface A_1 (black open circles), surface A_2 (red open triangles), and their sum (blue filled cubes). (d) SHG field components from surfaces B_1 and C_1 (black open circles), B_2 and C_2 (red open triangles) and their sum (blue filled cubes).

shorter than that of χ_{X1} . The numerical data reproduced the redshift of peak X'_1 with respect to peak X_1 , although the magnitude of the shift was smaller than that of the experimental data [Fig. 2(a)]. The second SHG peak at $\lambda'_{X2} = 790$ nm appeared slightly longer than the corresponding extinction peak at λ'_{X2} . The observation of the blue shift of peak X'_2 with respect to peak X_2 in the numerical SHG excitation spectra was also consistent with the experimental data in Fig. 2(a).

To study the SHG conversion process on each of the surfaces separately, the SHG field component generated on each

of the surfaces was calculated according to Eq. (3),

$$S_X = \int_X \chi_{\perp\perp\perp} \cdot E_{\perp}(\omega, \vec{r})^2 \cdot E_{\perp}(2\omega, \vec{r}) \cdot dS, \quad (3)$$

where $X (= A_1, A_2, B_1, B_2, C_1, \text{ and } C_2)$ is the surface of interest. The data were acquired 5 nm above each surface. Figure 4(c) shows the plots of components S_{A1} and S_{A2} and their sum ($S_{A1} + S_{A2}$) as functions of the excitation light wavelength. The term $S_{A1} + S_{A2}$ provides the total SHG wave component generated on the surfaces of the monomer moiety. Component S_{A1} was opposite in sign to S_{A2} and oscillated out of phase with S_{A2} . S_{A1} had two moderately large peaks at 950 and 790 nm, whereas S_{A2} had a large negative peak at 930 nm. The contribution of S_{A2} overwhelmed that of S_{A1} in the 930-nm wavelength region. Conversely, the nonlinear polarization was generated only on surface A_1 in the 790-nm wavelength region.

Figure 4(d) shows the component generated on the surfaces of the dimer moiety. Owing to the mirror symmetry in the $y-z$ plane, the amount of S_{B1} was identical to that of S_{C1} . For the same reason, the amount of S_{B2} equaled the amount of S_{C2} . In the figure, the amounts of $S_{B1} + S_{C1}$ and $S_{B2} + S_{C2}$ are shown together with the sum of $S_{B1} + S_{B2} + S_{C1} + S_{C2}$. $S_{B1} + S_{C1}$ was opposite in sign to $S_{B2} + S_{C2}$ because the former oscillated out of phase with respect to the latter.

$S_{B1} + S_{C1}$ had a positive peak at 930 nm, whereas $S_{B2} + S_{C2}$ had a negative peak at 900 nm. They both tended to tail off to shorter wavelengths. In the 930-nm wavelength region, the contribution of $S_{B1} + S_{C1}$ overwhelmed that of $S_{B2} + S_{C2}$. Furthermore, $S_{B1} + S_{C1}$ canceled $S_{B2} + S_{C2}$ almost perfectly, and their sum $S_{B1} + S_{B2} + S_{C1} + S_{C2}$ was almost zero in the 790-nm region. SHG conversions did not occur from the dimer moiety in the same wavelength region.

Next, the SHG conversions from the entire dolmen structure are discussed. In the 930-nm wavelength region, the nonlinear polarization was generated more efficiently in the nanogap area surrounded by surface A_2 , B_1 , and C_1 . $S_{A1} + S_{A2}$ of the monomer moiety was larger than $S_{B1} + S_{B2} + S_{C1} + S_{C2}$ of the dimer moiety. The SHG wave converted on surface A_2 interfered destructively with those on B_1 and C_1 , and the remaining SHG wave component was observed as far-field SHG signals.

In contrast, the peak wavelengths of S_{A1} , S_{B2} , and S_{C2} , the surfaces outside of the nanogap region, were inconsistent. The S_{A1} peak wavelength (954 nm) was much longer than the peak wavelengths of S_{B2} and S_{C2} (898 nm). At these wavelengths, the plasmon polarizations on the monomer and dimer moieties were somewhat weakly coupled to each other. The confinement of the surface charge in the nanogap was weakened. Simultaneously, it was distributed on the surfaces inside and outside nanogap. As a result, the intensity of the near fields increased and a certain amount of nonlinear polarizations was more likely to be generated on the surfaces A_1 , B_2 , and C_2 . The peak wavelength of the far-field SHG signals was shifted by the nonlinear polarization contributions outside the nanogap with respect to that of the linear extinction spectrum.

In the 790-nm wavelength region, the contribution of the monomer moiety, $S_{A1} + S_{A2}$, was substantial. Although the nonlinear polarization was locally present in the dimer moiety, it did not contribute to the far-field SHG signals. This occurred

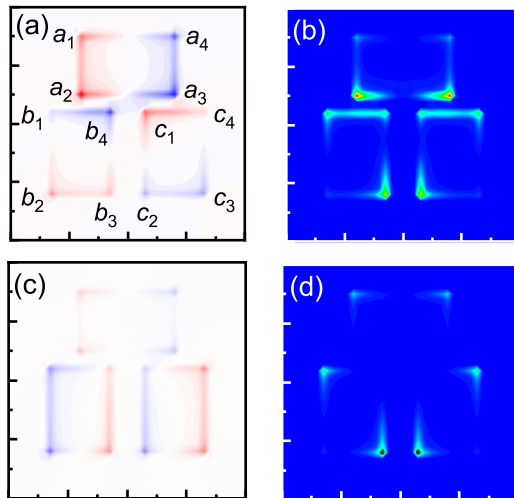


FIG. 5. Calculated charge density and near-field distributions of a dolmen-type Au nanostructure. Graphs (a) and (b) are the charge density and near-field at 910 nm, respectively. Graphs (c) and (d) are the data at 790 nm.

because the SHG wave from S_{B1} offsets the SHG wave from S_{B2} . The SHG wave from S_{C1} also offset the SHG wave from S_{C2} . The SHG waves propagate into the far field because of the nonlinear polarization generated on surface A_1

Yu *et al.* reported the observation of intense photoemission electron signals at the extinction peaks of both the bonding and antibonding hybridized states [43]; therefore, the intense SP-enhanced fields occurred in these modes. In the present study, the intense SHG signal was obtained at the extinction peaks of both the bonding and antibonding hybridized states. This result is consistent with that obtained using photoemission electron microscopy. However, the SHG signal caused by the bonding state was much higher than that caused by the antibonding state. Therefore, in addition to the field enhancement, a method of hybridization is necessary for efficient SHG conversion.

Our present paper does not simply experimentally test the prediction of the previous numerical study by Butet *et al.* in Ref. [22]. Our paper clearly shows which hybridized plasmon modes were the main contributors to the second-order nonlinear optical effects. The previous study analyzed the SHG behavior at the wavelength satisfying the so-called Fano-resonance. They calculated it monochromatically at the Fano dip, which corresponds to the valley between the two peaks in the linear spectrum. Conversely, our present paper does not find significant SHG conversion at the Fano dip. Rather, the intense SHG conversion behavior occurred near the extinction peak due to the bonding hybridized mode. This result indicates that the resonance to the bonding hybridized mode, rather than the Fano resonance, provides the unharmonicity suitable for the second-order NLO in the dolmen-type AuNR structure. It was only after we studied the spectrally resolved SHG data both experimentally and numerically that this physical insight was obtained.

The calculated surface charge and near-field distributions are presented to discuss the role of hybridized plasmon modes in generating the nonlinear polarization at each SHG peak

wavelength. Figures 5(a) and 5(b) show the surface charge and near-field distributions, respectively, at 910 nm. In the dimer moiety, the surface charges oscillated antisymmetrically in the two parallel AuNRs of the dimer moiety, exhibiting the electric quadrupole mode characteristics. These results confirm that the dipole mode in the monomer moiety and the quadrupole mode in the dimer moiety were hybridized in phase to form a bonding mode.

Intense near-field distributions were found in the nanogap region surrounded by surfaces A_2 , B_1 , and C_1 . They were most strongly distributed at the $a_2 - a'_2$ and $a_3 - a'_3$ edges on surface A_2 of the monomer moiety. The field intensity at these two edges was much higher than that at $a_1 - a'_1$ and $a_4 - a'_4$. The formation of the bonding hybridized plasmon mode promoted greater redistribution of the near fields inside the nanogap region than outside it in the monomer moiety. The moderately intense fields were widely distributed over the entire surfaces of B_1 and C_1 of the dimer moiety. This observation demonstrates that the electric force lines flowed between the $a_2 - a'_2$ edge and surface B_1 as well as between the $a_3 - a'_3$ edge and surface C_1 . The near-field distributions at the $b_3 - b'_3$ edge on surface B_2 and at the $c_2 - c'_2$ edge on surface C_2 were less intense and contributed little to the far-field SHG signals.

The nonlinear polarization generated in the nanogap region was mostly responsible for the far-field SHG signals. The near fields were linearly concentrated at the $a_2 - a'_2$ and $a_3 - a'_3$ edges on surface A_2 and were converted into SHG waves more efficiently than on surface B_1 and C_1 , on which the fields were widely dispersed. The SHG waves converted on A_2 interfered destructively with those converted on B_1 and C_1 , and the former overcame the latter, resulting in intense far-field SHG signals.

The near-field distribution was also calculated for the reference single AuNR structure at an extinction peak wavelength of 800 nm. The near field was equally distributed at the four edges of $a_1 - a'_1$, $a_2 - a'_2$, $a_3 - a'_3$, and $a_4 - a'_4$. The SP field enhancement factor ($\eta_{\text{mono}} = |E_{SP}^2|/|E_0|^2$) was 120 at these edge regions. Conversely, the SP field enhancement factor of the dolmen-type Au nanostructure (η_{dolmen}) was 480 at the $a_2 - a'_2$ and $a_3 - a'_3$ edges and 200 at the $a_1 - a'_1$ and $a_4 - a'_4$ edges, which were much higher than that of the reference. The enhanced SHG conversion efficiency in the dolmen-type Au nanostructure was a result of the noncentrosymmetric field distribution caused by the mode hybridization as well as the large field enhancement effect caused by the gap plasmon effect.

Figures 5(c) and 5(d) show the surface charge and near-field distributions at a wavelength of 790 nm. The surface charges oscillated antisymmetrically in the two parallel AuNRs of the dimer moiety, demonstrating the characteristics of the electric quadrupole plasmon mode. In contrast to the case at 910 nm, the dipole mode of the monomer moiety and the quadrupole mode of the dimer moiety were hybridized out-of-phase to form an antibonding state. In the monomer moiety, the surface charge density at the $a_1 - a'_1$ and $a_4 - a'_4$ edges was higher than that at the $a_2 - a'_2$ and $a_3 - a'_3$ edges in the monomer moiety. In the dimer moiety, the density at the $b_2 - b'_2$, and $c_3 - c'_3$ edges was higher than that at the $b_4 - b'_4$ and $c_1 - c'_1$ edges. The surface charge density was higher out-

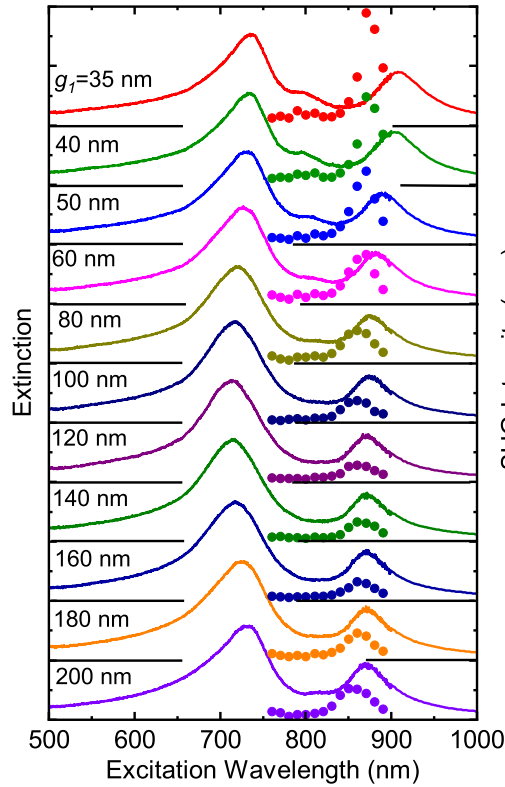


FIG. 6. Extinction (solid curves) and SHG excitation (filled circles) spectra of dolmen-type Au nanostructures with different edge-to-edge separations (g_1).

side than inside the nanogap. Owing to the repulsive Coulomb interactions between the monomer and dimer moieties, the flow of the electric force lines between surfaces A_1 and B_1 and between A_2 and C_1 was suppressed.

Near the $a_2 - a'_2$, $a_3 - a'_3$, $b_4 - b'_4$ and $c_1 - c'_1$ edges, there was almost no near-field distribution in the nanogap region. Rather, there was a moderately strong distribution near the $a_1 - a'_1$, $a_4 - a'_4$, $b_1 - b'_1$, $b_3 - b'_3$, $c_2 - c'_2$, and $c_4 - c'_4$ edges outside the nanogap region. Notably the near fields at the $b_1 - b'_1$ and $b_3 - b'_3$ edges were symmetrically distributed with respect to the center of the AuNR in the left part of the dimer moiety. The SHG waves generated at these two edges oscillated out-of-phase with one another, canceling each other as they propagated into the far field. Similarly, the near fields at the $c_2 - c'_2$ and $c_4 - c'_4$ edges were distributed symmetrically with respect to the center of the AuNR in the right part of the dimer moiety. They had almost no effect on the far-field SHG signals. For this reason, the nonlinear polarization components, $S_{B1} + S_{C1}$ and $S_{B2} + S_{C2}$, had opposite signs and their absolute values were approximately equal [Fig. 4(d)]. The weak SHG signal at 790 nm was attributed to the nonlinear polarizations generated at the $a_1 - a'_1$ and $a_4 - a'_4$ edges on the surface A_1 .

Finally, the dependence of linear and nonlinear optical behavior on the interparticle gap separation (g_1) is reported for the dolmen-type AuNR nanostructure. Figure 6 shows the extinction and SHG excitation spectra of the dolmen-type Au nanostructure with different g_1 values between 30 and 200 nm. The spectroscopic measurements were performed under x -

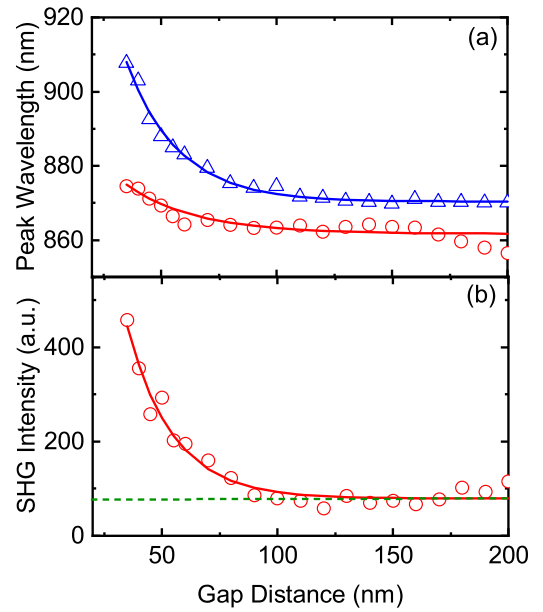


FIG. 7. (a) SHG (red open circles) and extinction (blue open triangles) peak wavelengths versus edge-to-edge separation (g_1). Solid curves are fitted to the exponential decay function. (b) SHG peak intensities versus g_1 .

polarized light. The intensity and position of the three peaks depended differently on g_1 .

As g_1 narrowed, the position of extinction peak X_1 , which corresponds to the bonding plasmon mode, became longer. This occurred because reduced separation caused stronger hybridizations of the plasmon modes. Extinction peak X_2 , which is related to the antibonding mode, was barely visible at $g_1 > 50$ nm. The position of extinction peak X_3 ($\lambda_{X3} \sim 735$ nm) was almost independent of g_1 . As shown in Fig. 2(a), the position of extinction peak was consistent with that of the reference dimer structure. This is because the interparticle plasmon coupling strength between the monomer and dimer moieties is weak in this mode.

In the SHG excitation spectrum, SHG peak X'_1 was observed near peak X_1 , regardless of g_1 . The SHG intensities increased as g_1 narrowed. As g_1 widened, the SHG intensities approached a constant value. This constant component of the SHG signal was attributed to the bulk term, which was related to the field gradient and originated mainly from the monomer moiety. The peak position of the SHG signal also became longer as g_1 became narrower.

For a more quantitative discussion, extinction peak λ_{X1} and SHG peak λ_{X1}' are plotted against g_1 in Fig. 7(a). The dependence of the peak wavelength on g_1 was well reproduced with a single-distance exponential decay function. The distance decay constant was $d_{\lambda, \text{Ext}} = 22 \pm 5$ nm for the extinction peak and $d_{\lambda, \text{SHG}} = 30 \pm 5$ nm for the SHG peak. The SHG peak intensity was also plotted against g_1 [Fig. 7(b)]. It was reproduced by the single-distance exponential decay function, and the distance decay constant is $d_{I, \text{SHG}} = 20 \pm 5$ nm. Although the values of $d_{\lambda, \text{Ext}}$, $d_{\lambda, \text{SHG}}$, and $d_{I, \text{SHG}}$ differed slightly, they remained consistent.

The plasmon coupling strength has been extensively studied for dimeric metal nanoparticle systems. According to

previous works, it is closely related to the magnitude of the redshift of the SP resonance wavelength with respect to that of the isolated nanoparticle [55,56]. A single exponential distance decay function is universally used to model the dependence of the spectral shift magnitude on the interparticle separation, independent of the particle shape, size, and environment.

Assuming that the plasmon coupling follows the purely electric dipole interaction model, the intensities of the near fields are inversely proportional to the cubic of the interparticle separations. In practice, higher-order multipolar terms, such as electric quadrupolar and octupolar, are involved [57]. Their distance dependencies obey the inverse power law with exponent $n > 3$. The decay of these terms is steeper than that of the cubic inverse relation of the dipole term. For example, the quadrupolar and octupolar decays are inversely proportional to the fourth and fifth powers of the interparticle separation, respectively. Because of the combined contributions of the different terms with different exponents, the decay behavior of the coupling strengths is well reproduced phenomenologically using an exponential decay function instead of the inverse power law. Previous studies have indicated that the gap-distance dependence of the near-field intensity follows a power-law rather than an exponential decay [58]. The current dependence of the SHG intensity on g_1 should be reproduced using a power law decay function. However, because of the constant term and the limited number of the data points, it is difficult to determine which of the model functions more accurately reproduces the experimental data. Here, the g_1 dependence of the SHG intensity was also reproduced using the exponential function to address the correspondence relationship with the peak wavelength shift.

In the previous studies, the decay distance constant was universally ~ 0.2 times the particle size and independent of types of the metals, the particle size, particle shape, and dielectric constant of the surrounding optical medium [58]. The width and length of the present AuNR were $W = 100$ nm and $L = 140$ or 160 nm, respectively. The distance decay constant

of ~ 20 – 30 nm was nearly equal to $15 \sim 20\%$ of the W and L . This universal rule is also useful to explain the plasmonic coupling strength in dolmen-type Au nanostructures. The present observations suggest that the appropriately hybridized mode provides the near-fields necessary for second-order nonlinear interactions. Furthermore, we found that the magnitude of the nonlinear susceptibilities at the nanoscale was flexibly controlled by g_1 .

V. CONCLUSIONS

This paper reports the SP-enhanced SHG behavior of the dolmen-type Au nanostructure. Because of its centrosymmetry, each constituent AuNR of this nanostructure by itself is unsuitable for second-order NLO and exhibits weak SHG conversion behavior. Conversely, the SHG intensity of the dolmen-type Au nanostructure was 25 times higher than that of the reference single AuNR. The dolmen-type Au nanostructure supports bonding and antibonding modes, which are hybridized between the electric dipole mode caused by the monomer moiety and the electric quadrupole mode caused by the dimer moiety. The numerical surface charge distribution shows that the enhanced SHG behavior is related to the hybridized bonding mode. The numerical data also indicate that the strong and confined near field in the nanogap region between the monomer and dimer moieties is noncentrosymmetric, resulting the enhanced far-field SHG signals. Additionally, the SHG signals were investigated as a function of the interparticle separation between the monomer and dimer moieties. The intensity and peak wavelength position of the SHG signals followed an exponential distant decay function. Their decay behavior was consistent with that of the extinction peak wavelength. The SHG conversions were found to occur extensively at interparticle separations less than $\sim 20\%$ of the AuNR. This paper demonstrates that the optical fields suitable for second-order nonlinear plasmonics can be engineered by appropriately arranging the centrosymmetric metal nanoparticles.

-
- [1] P. G. Kik and M. L. Brongersma, *Surface Plasmon Nanophotonics* (Elsevier, Dordrecht, 2007), Chap. 1, pp. 1–36.
- [2] S. A. Maier, *Plasmonics Fundamentals and Applications* (Springer, New York, 2007), Chap. 5, pp. 65–88
- [3] I. R. Hooper and W. L. Barnes, *Modern Plasmonics* (Elsevier, Amsterdam, 2014), Chap. 1, pp. 1–36.
- [4] V. Amendola, R. Pilot, and M. Frasconi, Surface plasmon resonance in gold nanoparticles: A review, *J. Phys.: Condens. Matter* **29**, 203002 (2017).
- [5] S. Gwo, H.-Y. Chen, M.-H. Lin, L. Sun, and X. Li, Nano manipulation and controlled self-assembly of metal nanoparticles and nanocrystals for plasmonics, *Chem. Soc. Rev.* **45**, 5672 (2016).
- [6] K. M. Mayer and J. H. Hafner, Localized surface plasmon resonance sensors, *Chem. Rev.* **111**, 3828 (2011).
- [7] A. M. Shrivastav, U. Cvelbar, and I. Abdulhalim, A comprehensive review on plasmonic-based biosensors used in viral diagnostics, *Commun. Biol.* **4**, 70 (2021).
- [8] Q. Wang, Z.-H. Ren, W.-M. Zhao, L. Wang, X. Yan, A. Song Zhu, F. mei Qiu, and K.-K. Zhang, Research advances on surface plasmon resonance biosensors, *Nanoscale* **14**, 564 (2022).
- [9] S. Link and M. A. El-Sayed, Size and temperature dependence of the plasmon absorption of colloidal gold nanoparticles, *J. Phys. Chem. B* **103**, 4212 (1999).
- [10] R. Jin, Y. Cao, C. A. Mirkin, K. L. Kelly, G. C. Schatz, and J. G. Zheng, Photoinduced conversion of silver nanospheres to nanoprisms, *Science* **294**, 1901 (2001).
- [11] M. W. Knight, Y. Wu, J. B. Lassiter, P. Nordlander, and N. J. Halas, Substrates matter: Influence of an adjacent dielectric on an individual plasmonic nanoparticle, *Nano Lett.* **9**, 2188 (2009).
- [12] X. Z. Wei and P. Mulvaney, *Modern plasmonics* (Elsevier, Amsterdam, 2014), Chap. 3, pp. 75–107.
- [13] N. J. Halas, S. Lal, W.-S. Chang, S. Link, and P. Nordlander, Plasmons in strongly coupled metallic nanostructures, *Chem. Rev.* **111**, 3913 (2011).

- [14] J. A. Fan, C. Wu, F. K. Bao, J. B. R. Bardhan, N. J. Halas, V. N. Manoharan, P. Nordlander, G. Shvets, and F. Capasso, Self-assembled plasmonic nanoparticle clusters, *Science* **328**, 1135 (2010).
- [15] P. Nordlander, C. Oubre, E. Prodan, K. Li, and M. I. Stockman, Plasmon hybridization in nanoparticle dimers, *Nano Lett.* **4**, 899 (2004).
- [16] E. Prodan, C. Radloff, N. J. Halas, and P. Nordlander, A hybridization model for the plasmon response of complex nanostructures, *Science* **302**, 419 (2003).
- [17] S. Y. Lee, L. Hung, G. S. Lang, J. E. Cornett, I. D. Mayergoyz, and O. Rabin, Dispersion in the SERS enhancement with silver nanocube dimers, *ACS Nano* **4**, 5763 (2010).
- [18] W. Li, P. H. C. Camargo, X. Lu, and Y. Xia, Dimers of silver nanospheres: Facile synthesis and their use as hot spots for surface-enhanced raman scattering, *Nano Lett.* **9**, 485 (2009).
- [19] J. B. Lassiter, H. Sobhani, J. A. Fan, J. Kundu, F. Capasso, P. Nordlander, and N. J. Halas, Fano resonances in plasmonic nanoclusters: Geometrical and chemical tunability, *Nano Lett.* **10**, 3184 (2010).
- [20] M. Kauranen and A. V. Zayats, Nonlinear plasmonics, *Nat. Photonics* **6**, 737 (2012).
- [21] S. B. Hasan, F. Lederer, and C. Rockstuhl, Nonlinear plasmonic antennas, *Mater. Today* **17**, 478 (2014).
- [22] J. Butet, P. F. Brevet, and O. J. F. Martin, Optical second harmonic generation in plasmonic nanostructures: From fundamental principles to advanced applications, *ACS Nano* **9**, 10545 (2015).
- [23] A. Krasnok, M. Tymchenko, and A. Alù, Nonlinear metasurfaces: A paradigm shift in nonlinear optics, *Mater. Today* **21**, 8 (2018).
- [24] B. Metzger, L. Gui, J. Fuchs, D. Floess, M. Hentschel, and H. Giessen, Strong enhancement of second harmonic emission by plasmonic resonances at the second harmonic wavelength, *Nano Lett.* **15**, 3917 (2015).
- [25] R. W. Boyd, *Nonlinear Optics*, 3rd ed. (Academic Press, Cambridge, 2007), Chap. 1, pp. 1–67.
- [26] B. K. Canfield, S. Kujala, K. Jefimovs, Y. Svirko, J. Turunen, and M. Kauranen, A macroscopic formalism to describe the second-order nonlinear optical response of nanostructures, *J. Opt. A: Pure Appl. Opt.* **8**, S278 (2006).
- [27] F. X. Wang, F. J. Rodriguez, W. M. Albers, R. Ahorinta, J. E. Sipe, and M. Kauranen, Surface and bulk contributions to the second-order nonlinear optical response of a gold film, *Phys. Rev. B* **80**, 233402 (2009).
- [28] C. Ciraci, E. Poutrina, M. Scalora, and D. R. Smith, Second-harmonic generation in metallic nanoparticles: Clarification of the role of the surface, *Phys. Rev. B* **86**, 115451 (2012).
- [29] J. E. Sipe, V. C. Y. So, M. Fukui, and G. I. Stegeman, Analysis of second-harmonic generation at metal surfaces, *Phys. Rev. B* **21**, 4389 (1980).
- [30] J. I. Dadap, J. Shan, and T. F. Heinz, Theory of optical second-harmonic generation from a sphere of centrosymmetric material: Small-particle limit, *J. Opt. Soc. Am. B* **21**, 1328 (2004).
- [31] J. Butet, J. Duboisset, G. Bachelier, I. Russier-Antoine, E. Benichou, C. Jonin, and P.-F. Breve, Optical second harmonic generation of single metallic nanoparticles embedded in a homogeneous medium, *Nano Lett.* **10**, 1717 (2010).
- [32] M. D. McMahon, R. Lopez, R. F. Haglund, E. A. Ray, and P. H. Bunton, Second-harmonic generation from arrays of symmetric gold nanoparticles, *Phys. Rev. B* **73**, 041401(R) (2006).
- [33] M. Finazzi, P. Biagioni, M. Celebrano, and L. Duò, Selection rules for second-harmonic generations in nanoparticles, *Phys. Rev. B* **76**, 125414 (2007).
- [34] B. K. Canfield, H. Husu, J. Laukkanen, B. Bai, M. Kuittinen, J. Turunen, and M. Kauranen, Local field asymmetry drives second-harmonic generation in noncentrosymmetric nanodimers, *Nano Lett.* **7**, 1251 (2007).
- [35] K. Thyagarajan, S. Rivier, A. Lovera, and O. J. F. Martin, Enhanced second-harmonic generation from double resonant plasmonic antennae, *Opt. Express* **20**, 12860 (2012).
- [36] M. Celebrano, X. Wu, M. Baselli, S. G. ßmann, P. Biagioni, A. Locatelli, C. D. Angelis, G. Cerullo, R. Osellame, B. Hecht, L. Duò, F. Ciccacci, and M. Finazzi, Mode matching in multiresonant plasmonic nanoantennas for enhanced second harmonic generation, *Nat. Nanotechnol.* **10**, 412 (2015).
- [37] K. Thyagarajan, J. Butet, and O. J. F. Martin, Augmenting second harmonic generation using Fano resonances in plasmonic systems, *Nano Lett.* **13**, 1847 (2013).
- [38] V. Niels, Y. Sonnefraud, H. Sobhani, F. Hao, V. V. Moshchalkov, P. V. Dorpe, P. Nordlander, and S. A. Maier, Resonances in individual coherent plasmonic nanocavities, *Nano Lett.* **9**, 1663 (2009).
- [39] J. Butet and O. J. F. Martin, Nonlinear plasmonic nanorulers, *ACS Nano* **8**, 4931 (2014).
- [40] B. Metzger, T. Schumacher, M. Hentschel, M. Lippitz, and H. Giessen, Third harmonic mechanism in complex plasmonic Fano structures, *ACS Photonics* **1**, 471 (2014).
- [41] T. Coenen, D. T. Schoen, S. A. Mann, S. R. K. Rodriguez, B. J. M. Brenny, A. Polman, and M. L. Brongersma, Nanoscale spatial coherent control over the modal excitation of a coupled plasmonic resonator system, *Nano Lett.* **15**, 7666 (2015).
- [42] V. Flauraud, G. D. Bernasconi, J. Butet, M. Mastrangeli, D. T. L. Alexander, O. J. F. Martin, and J. B. Brugger, Mode evolution in strongly coupled plasmonic dimers fabricated by templated assembly, *ACS Photonics* **4**, 1661 (2017).
- [43] V. Yu, Q. Sun, K. Ueno, T. Oshikiri, A. Kubo, Y. Matsuo, and H. Misawa, Exploring coupled plasmonic nanostructures in the near field by photoemission electron microscopy, *ACS Nano* **10**, 10373 (2016).
- [44] C. Yan and O. J. F. Martin, Periodicity-induced symmetry breaking in a Fano lattice: Hybridization and tight-binding regimes, *ACS Nano* **8**, 11860 (2014).
- [45] B. Lamprecht, G. Schider, R. T. Lechner, H. Ditlbacher, J. R. Krenn, A. Leitner, and F. R. Aussenegg, Metal Nanoparticle Gratings: Influence of Dipolar Particle Interaction on the Plasmon Resonance, *Phys. Rev. Lett.* **84**, 4721 (2000).
- [46] C. L. Haynes, A. D. McFarland, L. L. Zhao, R. P. V. Duyne, G. C. Schatz, L. Gunnarsson, J. Prikulis, B. Kasemo, and M. Kall, Nanoparticle optics: the importance of radiative dipole coupling in two-dimensional nanoparticle arrays, *J. Phys. Chem. B* **107**, 7337 (2003).
- [47] K. Yee, Numerical solution of initial boundary value problems involving Maxwell's equations in isotropic media, *IEEE Trans. Antennas Propag.* **14**, 302 (1966).
- [48] K. O'Brien, H. Suchowski, J. Rho, A. Salandrino, and B. Kante, Predicting nonlinear properties of metamaterials from the linear response, *Nat. Mater.* **14**, 379 (2015).

- [49] J. Butet and O. J. F. Martin, Evaluation of the nonlinear response of plasmonic metasurfaces: Miller's rule, nonlinear effective susceptibility method, and full-wave computation, *J. Opt. Soc. Am. B* **33**, A8 (2016).
- [50] S. Roke, M. Bonn, and A. V. Petukhov, Nonlinear optical scattering: The concept of effective susceptibility, *Phys. Rev. B* **70**, 115106 (2004).
- [51] G. Bachelier, J. Butet, I. Russier-Antoine, E. B. C. Jonin, and P.-F. Brevet, Origin of optical second-harmonic generation in spherical gold nanoparticles: Local surface and nonlocal bulk contributions, *Phys. Rev. B* **82**, 235403 (1972).
- [52] P. B. Johnson and R. W. Christy, Optical constants of the noble metals, *Phys. Rev. B* **6**, 4370 (1972).
- [53] A. Belardini, M. C. Larciprete, E. F. M. Centini, C. Sibilìa, M. Bertolotti, A. Toma, D. Chiappe, and F. B. de Mongeot, Tailored second harmonic generation from self-organized metal nanowires arrays, *Opt. Express* **17**, 3603 (2009).
- [54] J. A. H. van Nieuwstadt, M. Sandtke, R. H. Harmsen, F. B. Segerink, J. C. Prangsma, S. Enoch, and L. Kuipers, Strong Modification of the Nonlinear Optical Response of Metallic Subwavelength Hole Arrays, *Phys. Rev. Lett.* **97**, 146102 (2006).
- [55] K.-H. Su, Q.-H. Wei, X. Zhang, J. J. Mock, D. R. Smith, and S. Schultz, Interparticle coupling effects on plasmon resonances of nanogold particles, *Nano Lett.* **3**, 1087 (2003).
- [56] P. Jain, W. Huang, and M. A. El-Sayed, On the universal scaling behavior of the distance decay of plasmon coupling in metal nanoparticle pairs: A plasmon ruler equation, *Nano Lett.* **7**, 2080 (2007).
- [57] P. K. Jain and M. A. El-Sayed, Plasmonic coupling in noble metal nanostructure, *Chem. Phys. Lett.* **487**, 153 (2010).
- [58] Y. Huang, Q. Zhou, M. Hou, L. Maa, and Z. Zhang, Nanogap effects on near- and far-field plasmonic behaviors of metallic nanoparticle dimers, *Phys. Chem. Chem. Phys.* **17**, 29293 (2015).